Chapter 5

Structural and Electrochemical Properties of Cementitious and Hybrid Materials Based on Nacrite

Nouha Jaafar, Hafsia Ben Rhaiem and Abdesslem Ben Haj Amara

Additional information is available at the end of the chapter

http://dx.doi.org/10.5772/61594

Abstract

This chapter gives possible valorization of a well-crystallized Tunisian nacrite as an interesting clay mineral belonging to the kaolin group: The first part of the chapter aims to produce a new synthetic material labeled ''metanacrite". Metanacrite is a supplementary cementitious material originated by heating a raw Tunisian nacrite at 823 K. The structure of the amorphous synthetic product was corroborated by X-ray diffraction (XRD) and infrared spectroscopy (IR). The decomposition of the silicate framework was confirmed by transmission electron microscope (TEM). The obtained metanacrite was also examined by electrochemical impedance spectroscopy (EIS). Accordingly, a semiconductor behavior of the novel synthetic material is evidenced. The second part of this chapter deals with the intercalation of lithium chloride salt between the planar layers of this Tunisian nacrite. The intercalation leads to a stable hybrid material that after calcination under inert atmosphere at 723–873 K induces an amorphous hybrid. The structural identification of the obtained nacrite–LiCl hybrid was determined by means of XRD, IR, TGA, and EIS. Finally, the resulting amorphous hybrid shows a superionic behavior with high ionic conductivity up to 10^{-2} S.m^{-1}, good electrochemical stability, and can be used as an innovative solid electrolyte in lithium batteries and other electrochemical devices.

Keywords: Nacrite, Clay Mineral, Metanacrite, Hybrid, Lithium-Ion Battery

1. Introduction

Clay minerals are abundant in soil and important to a wide variety of disciplines such as environmental chemistry, astrophysics, geology, and the ceramics industry [1]. One of the most

used clay minerals is **kaolin,** which is a 1:1 dioctahedral layered aluminosilicate produced of advanced weathering processes [2]. Kaolin clays include kaolin-group minerals, of which the most common are kaolinite, dickite, nacrite, and halloysite [3]. Kaolin is white or near white color with pseudo-hexagonal crystal along with plates, some larger books, and vermicular stacks [4]. The structural formula of kaolin is $[Al_2Si_2O_5(OH)_4]$ per half unit cell with Si/Al ratio ~. 1One layer of the mineral consists of an alumina octahedral sheet and a silica tetrahedral sheet that share a common plane of oxygen atoms and repeating layers of the mineral are hydrogen bonded together [2,5]. Quantitative estimates indicate that the cohesive energy between kaolinite layers is primarily electrostatic [6]. There is also a certain degree of van der Waals attraction between the hydroxyl groups of the gibbsite sheet and the oxygen atoms of the adjoining silica sheet [7, 8].

Consequently, wide applications based on virgin as well as treated (heat treatment, functionalization, etc.) kaolinite were developed:

1. Clay minerals in soil play an important role in the environment by acting as a natural scavenger of pollutants from water through adsorption mechanism [9]. For example, China clay can confiscate cadmium from hazardous waste [10]. Use of kaolinite for the removal of copper, nickel, cobalt, and manganese is also studied [11].

2. Conversion of kaolin to metakaolin by firing above the dehydroxylation temperature activates the clay and improves its properties [12]. The heating process drives off water from the mineral ($Al_2O_3 \cdot 2SiO_2 \cdot 2H_2O$), the main constituent of kaolin clay, and collapses the material structure, resulting in an amorphous aluminosilicate ($Al_2O_3 \cdot 2SiO_2$), metakaolin. Metakaolin (MK) had 99.9% particles <16 μm with a mean particle size of about 3 μm (www.metakaolin.com). Therefore, there is an ongoing interest to apply metakaolin in the construction industry as a raw material for the production of white cement clinker and as an artificial pozzolanic additive for concrete to produce blended cement [4]. The use of by-products like metakaolin in cement and concrete has gained significant importance because of the requirements of environmental protection and sustainable construction in the future [13].

3. The ability to modify clay minerals by insertion of inorganic and/or organic guest species into the interlamellar region opens up a range of potential uses for these materials. The resultant hybrid materials combine the features of the clay and the guest species. These complexes have the potential to be used as adsorbents, as catalyst support, and in chromatographic columns and ion exchangers [14].

In this regard, Tunisian nacrite has been employed as a natural clay mineral in the development of new materials with high functionalities and unique properties. Therefore, the first part of this study herein describes the structural and electrochemical characteristics of a novel material, commonly named "*metanacrite*". This chapter allows us to achieve better applicability of the calcined nacrite, as a supplementary cementitious material (SCM) that can be used to replace part of the clinker in a cement or cement in a concrete mixture. The second part of this work deals with the control of the evolution of the nacrite structure during the intercalation process and the study of the structural and electrochemical properties of the novel synthesized material labeled "*nacrite–LiCl nanohybrid*".

2. Tunisian nacrite: Starting clay mineral

Well-crystallized Tunisian nacrite from North Tunisia (Jbel Slata, Kef) was used in this work as a starting clay mineral economically viable and technically efficient [15]. This layered aluminosilicate material contributes large particle size and high chemical stability and has been previously characterized in the work of Ben Haj Amara and co-workers [15–21]. Bailey [22] described nacrite by a 2M stacking mode which crystallized in the monoclinic lattice with a Cc space group. The structural parameters of nacrite are $a = 0.8906$ nm, $b = 0.5146$ nm, $c = 1.5669$ nm, and $\beta = 113.58°$ with a main basal distance $d_{002} = c \sin \beta/2 = 0.72$ nm [15, 19].

3. Dehydroxylation of nacrite: Metanacrite

Recently, several studies focused on the physicochemical characteristics of *metakaolin* (MK) materials derived from dehydroxylation of *kaolin* at 823 K. This phenomenon is accompanied by loss of water and decomposition into a disordered metastate [23], which undergoes massive structural changes of the octahedral layer: aluminium changes its coordination from six to four and five [24–26]. In Tunisia, particular attention is given to the exploitation of clays which are abundant in the country and may present potential pozzolanic activity, if they are appropriately calcined at relatively low temperatures [27, 28].

3.1. Calcination procedure

The sample of about 20 g was heat treated in the "Nabertherm GmbH" laboratory furnace. The optimal calcination parameters, for which complete dehydroxylation of the material was achieved, are temperature of 823 K and heating time of 120 min. The dehydroxylation process may be presented by the following simple equation [29]:

$$\underset{\text{nacrite}}{Al_2O_3.2SiO_2.2H_2O} \rightarrow \underset{\text{metanacrite}}{Al_2O_3.2SiO_2} + \underset{\text{water}}{2H_2O}.$$

3.2. Structural Properties of Tunisian Metanacrite

3.2.1. X-Ray Diffraction

The experimental X-ray diffraction patterns of both nacrite and metanacrite are reported in Figures 1(a) and 1(b), respectively. Results show a broad characteristic reflection extending from approximately 17 to 39°2θ attributed to the overlapping of the 00l reflections of the well-crystallized natural nacrite [15–21]. The XRD analysis illustrates then the amorphous structure of the obtained metanacrite synthetic phase [29].

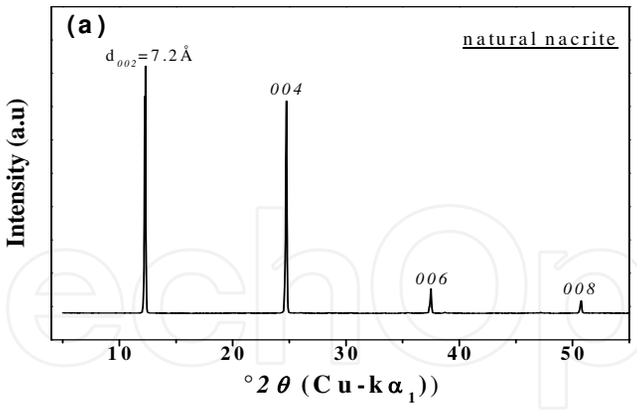

(a)

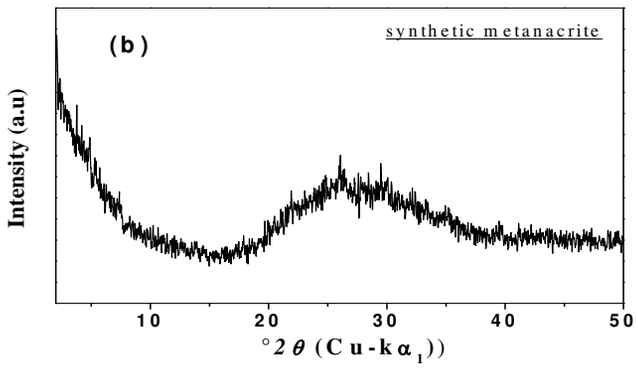

(b)

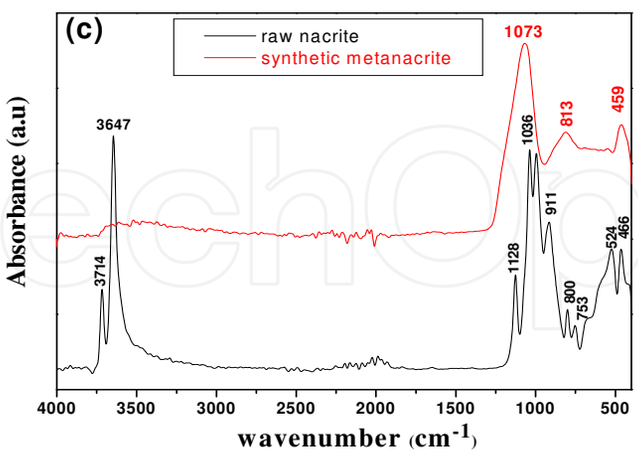

(c)

Figure 1. (a) Experimental X-ray pattern of nacrite raw-clay material [29]. (b) Experimental X-ray pattern of metanacrite synthetic material [29]. (c)Infrared spectra in the 4000–400 cm^{-1} region for nacrite and metanacrite samples [29].

http://dx.doi.org/10.5772/61594

3.2.2. IR Spectroscopy

By comparing the IR spectra of metanacrite and nacrite recorded in Figure 1(c), it is possible to follow the modifications of the stretching and deformation vibrations obtained after heating nacrite above 823 K: they shift from their positions in the spectrum of untreated nacrite, and their shapes change. Indeed, *at high frequencies*, it should be mentioned that no bands were detected in the infrared spectrum of metanacrite, indicating the disappearance of the OH lattice stretching band since it is located in the envelope of water band corresponding to natural nacrite at 3714 and 3647 cm^{-1} [15, 17–21]. Figure 1(c) reveals that, *at low frequencies*, the Si–O stretching vibrations υ(Si–O) located at 1073 cm^{-1} and the Si–O deformation vibrations located at 459 cm^{-1} are commonly present with a slight change in their shape and intensity, while the Al–O deformation vibrations are shifted to high frequencies from 524 to 813 cm^{-1} and the Al–OH deformation vibrations placed at 753, 800, and 911 cm^{-1} in the spectrum of nacrite are omitted in the spectrum of metanacrite. All these changes in the infrared spectrum between metanacrite and nacrite imply that the starting aluminosilicate loses water during calcinations. The layered structure is then destroyed and transformed into a disordered metanacrite phase possessing amorphous structure very different from the nacrite matrix [29].

3.2.3. TEM and EDXS

The morphology, size, and composition of the synthesized sample were characterized via local chemical microanalysis performed using energy dispersive X-ray spectroscopy (EDXS) coupled to the transmission electron microscope (TEM). Figure 2 provides the TEM observations micrographs of Tunisian metanacrite. At first glance, the studied sample exhibits a disordered granular structure with various shapes and sizes. We note the presence of defects, mostly dislocations, which are generated by the distortion around the particle. The contributions of defects, grain size, distribution, and morphology confirm that the amorphous behavior dominates the whole structural composition of metanacrite synthetic material. Such defects seem to be produced during the heating of the starting nacrite clay material and play an important role in the second part of this paper. The larger the number of defects and disorder, the higher the mobility of the free charge carriers, which results in an improvement of the conduction behavior. In order to obtain more detailed information about the microstructure and the chemical composition of metanacrite, we performed *TEM* coupled with *EDXS* analysis. The obtained spectra show the presence of Si and Al atoms with a major proportion, constituting the fundamental elements of the metanacrite phase, with a minor contribution of Fe and Cu atoms corresponding to the presence of a trace amount of impurities in the metanacrite material. However, the presence of Ni atoms belongs to the membrane on which the sample is placed. The preliminary physicochemical analysis of metanacrite reveals that the sample is mainly in high amorphous aluminosilicate phase with a disordered polymerized silicon/aluminum framework which allows its applicability as a new synthetic source of pozzolan for producing composite building materials [29].

3.3. Electrochemical properties of Tunisian Metanacrite

In order to investigate the role of the microstructure of the resultant amorphous synthetic material in the transport properties, we carried out electrochemical impedance spectroscopy

(EIS). The impedance measurements were taken in an open circuit in the frequency range from 10 Hz to 13 MHz, with an applied potential of 50 mV at different temperatures. The metanacrite sample was ground to fine powder and pressed into a pellet. Platinum electrodes were deposited by sputtering on both parallel faces of the pellet to form a symmetrical cell. The cell was then placed inside a programmable oven coupled with a temperature controller [29, 30].

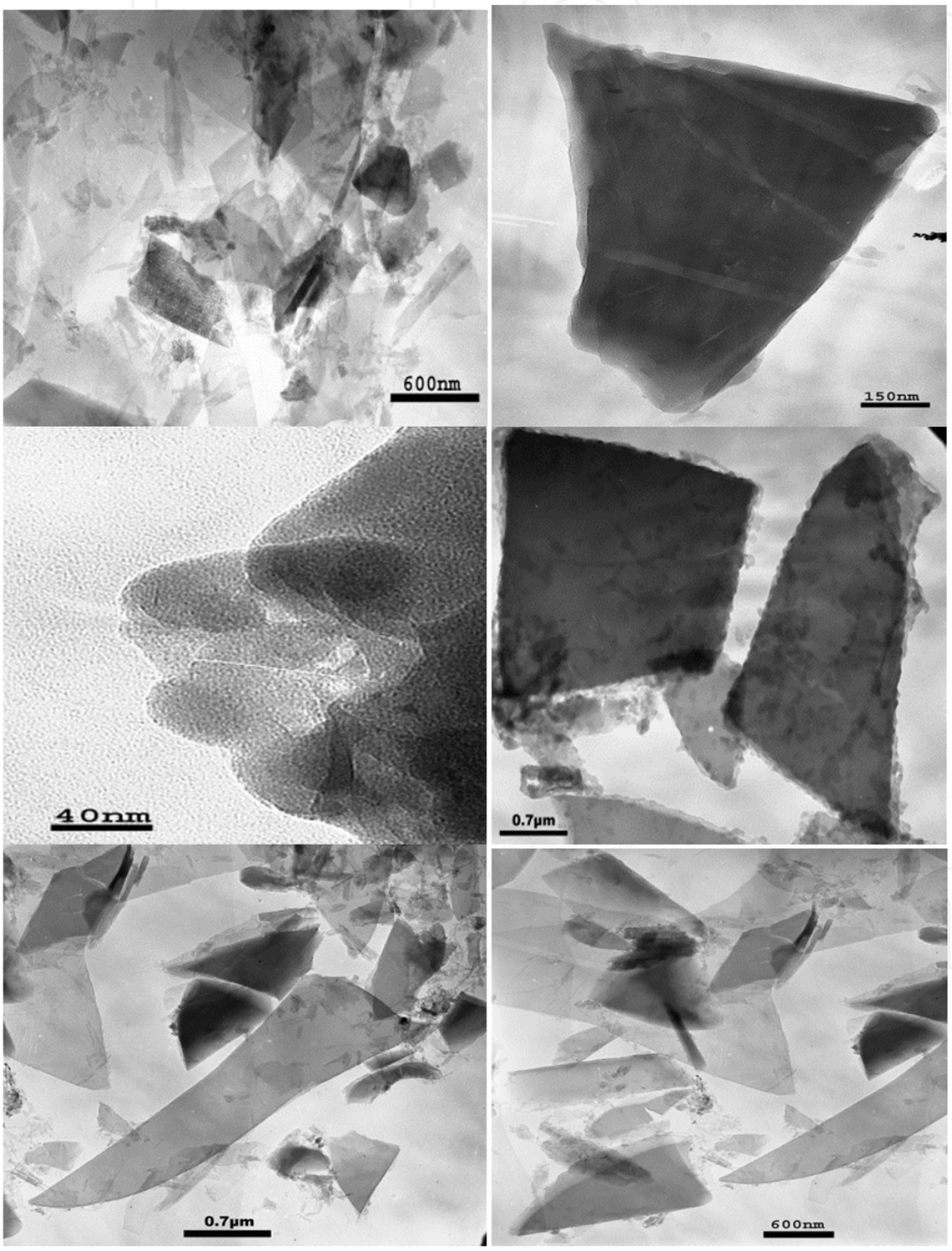

Figure 2. TEM micrographs of metanacrite synthetic material [29].

http://dx.doi.org/10.5772/61594

3.3.1. Impedance Analysis

In this section, we will discover the influence of the heat treatment of metanacrite from room temperature to 873 K on the enhancement of the electrical conductivity. Accordingly, the complex impedance plots of metanacrite in the temperature range 298–873 K are displayed in Figure 3.

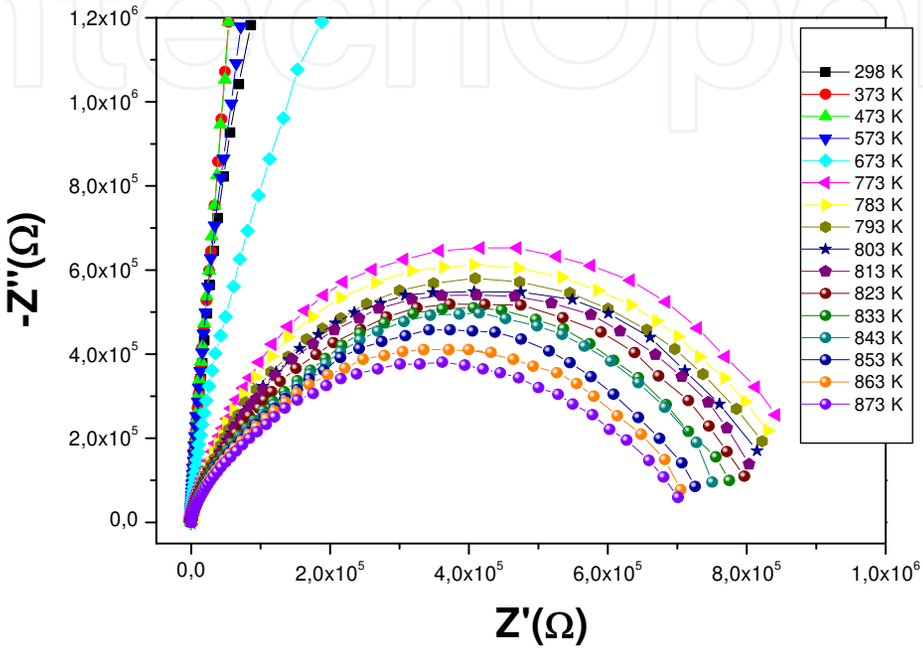

Figure 3. Nyquist diagram of metanacrite at the temperature range from 298 to 873 K [29].

The Nyquist plots describe the transport properties which are strongly affected by the microstructure. From Figure 3, two domains are identified: the first one is observed at low temperature (298–673 K) describing the insulator behavior and the second one is detected at high temperature (673–873K) for which a significant increase in conductivity is observed. The increase of the electrical conductivity may be attributed to an increase of the disorder degree as well as defects density in the sample [29].

3.3.2. Electrical conductivity

Different models have been proposed to describe and draw the ac conduction model corresponding to metanacrite such as quantum mechanical tunneling (Q.M.T.) [31,32], non-overlapping small-polaron tunneling (N.S.P.T), overlapping large-polaron tunneling (O.L.P.T.), and the correlated barrier hopping (C.B.H.) [31–36]. All these models were deemed to be in disagreement with our results. Therefore, the experimental data will be discussed in the frame of the C.B.H. model. Thus, the conduction occurs via the hopping carriers over a potential barrier between two different valence states. The ac conductivity and frequency exponent expressions due to the C.B.H. model are given by the following equations:

$$s_{ac}(\omega) = \left(\frac{1}{24}\right) \pi^3 \varepsilon' N^2 \varepsilon_0 \omega R^6 \tag{1}$$

$$s = 1 - \left\{ \frac{6kT}{W_M + k_B T \ ln\left(1/\omega\tau_0\right)} \right\} \tag{2}$$

where σ_{ac} is the ac conductivity, ε_0 is the free-space dielectric permittivity, is the dielectric constant, N is the density of states at Fermi level, R_ω is the hopping length at frequency ω, W_M is the maximum barrier height, τ_0 the atomic vibration period, s is the frequency exponent, and k_B is the Boltzmann constant.

Equation (2) predicts that s decreases with increasing temperature. Therefore, the C.B.H. is the involved conduction mechanism for the investigated metanacrite sample [37, 38].

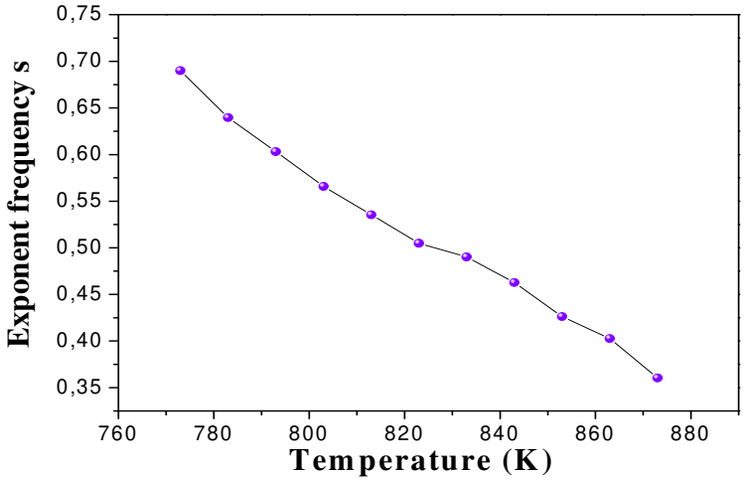

Figure 4. Temperature dependence of frequency exponent(s) for metanacrite sample [29].

Concerning the ac conductivity of metanacrite, it is found to obey the universal Arrhenius power law [39]:

$$\sigma_{ac} = \sigma_0 \exp\left(\frac{-E_{a(ac)}}{k_B T}\right) \tag{3}$$

where σ_0 is the pre-exponential factor, k_B is the Boltzmann constant, T is the temperature, and $E_{a(ac)}$ is the activation energy that controls the jump of charge carriers from one site to another neighboring site. The (ac) values have been calculated at four fixed frequencies [29]. Indeed, the activation energy varies between 0.24 ± 0.01 eV (at low frequencies) and 0.17 ± 0.01 eV (at high frequencies). These results are specific to the temperature range 773–873 K. Thus, the increase of the applied frequency enhances the electronic jumps between the localized states.

Consequently, the activation energy decreases with increasing frequency. Moreover, at high frequency, the ac activation energies are found to be lower than those found at low frequency regions [29]. Therefore, at high frequencies the mobility of charge carriers over short distances needs lower energy than that necessary for mobility over longer distances at low frequencies.

The ac conductivity increases as a function of frequency at a fixed temperature (773 K) from $3.40 \cdot 10^{-6}$ S·m^{-1} at f =100 Hz to $1.27 \cdot 10^{-2}$ S·m^{-1} at f = 10 MHz [29]. Besides the ac conductivity increases as a function of temperature at a fixed frequency (f = 10 MHz), it increases from $1.27 \cdot 10^{-2}$ S·m^{-1} at T = 773K to $1.98 \cdot 10^{-2}$ S·m^{-1} at T = 873 K. The small values of the ac activation energy $E_{a(ac)}$ and the increase of ac conductivity σ_{ac} with the increase of frequency confirm the dominant hopping conduction mechanism.

The conductivity is thermally activated; therefore, the electrical conduction follows a process in which the electron or hole hops from one localized site to another. The electron resides at one site; when it is thermally activated, it migrates to another site. Moreover, we demonstrated in the first part of this chapter that the defects constitute the active sites in the conduction process. Therefore, the electron or hole tends to associate with local defects, so the activation energy for charge transport may also include the energy of freeing the hole from its position next to the defect [40]. Otherwise, the electronic conduction takes place by hopping between two charge-defect states over the barrier separating them.

As mentioned above, the ac conductivity increases with increasing both temperature and frequency. Simultaneously, the dc conductivity increases with increasing temperature (Figure 5). Indeed, the dc conductivity (σ_{dc}) fits the well-known Arrhenius relation [39]. We found $E_{a(dc)}$ = 0.24 ± 0.01 eV (Figure 5):

$$\sigma_{dc} = \frac{\sigma_0}{T} \exp\left(\frac{-E_{a(dc)}}{k_B T}\right) \tag{4}$$

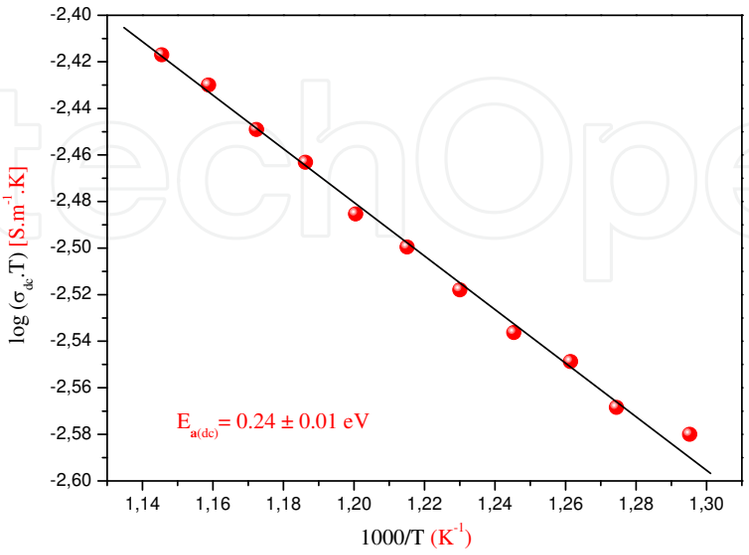

Figure 5. Evolution of the *dc* conductivity of metanacrite between 773 K and 873K [29].

where σ_0 is the pre-exponential factor, $E_{a(ac)}$ is the activation energy, T is the temperature, and k_B is the Boltzmann constant. As a consequence of the increased dc conductivity with temperature for small activation energies, we conclude that the amorphous metanacrite sample behaves like a semiconductor material [29].

From these results, we deduce a correlation between the electrochemical impedance spectroscopy and the structural properties of amorphous Tunisian metanacrite synthetic material.

4. Functionalization of Nacrite: Nacrite–LiCl Nanohybrid

Intercalation of kaolin nanoclay minerals with inorganic and organic compounds has wide potential for scientific and industrial applications [41]. Indeed, intercalation is eventually accompanied by substantial modifications of the kaolin surface due to the expansion of the interlamellar space [42,43]. The resulting hybrid materials have attracted much interest from researchers, since they frequently show unexpected and remarkable improvements in the rheological, mechanical, thermal, optical, and electrical properties compared to the unmodified aluminosilicate clay mineral.

However, due to the hydrogen-bonding between the layers of kaolinite, only a limited number of small and highly polar organic compounds such as dimethyl-sulfoxide, deuterated dimethyl-sulfoxide [44], formamide [45], N-methylformamide (NMF), dimethylformamide, acetamide, pyridine N-oxide, potassium acetate, and methanol can directly be intercalated [46, 47]. Thus, these kaolinite intercalation compounds were used as precursors, because intercalation reactions of kaolinite have been extended by a guest displacement method in which a new guest can be intercalated by displacing previously intercalated species [48]. Additionally, three intercalation modes of alkali halides into the kaolin subgroup can be distinguished [49]: Mode A includes those species that are directly intercalated [50, 51]. Mode B includes those species which can enter the interlayer space by means of an "entraining agent" such as hydrazine or ammonium acetates [52]. Mode C includes those species which can only be intercalated into the interlayer space by the displacement of a previously intercalated compound such as dimethylsulfoxide "DMSO" [52].

In the case of Tunisian nacrite-polytype, the intercalation process of several inorganic salts and dipolar organic molecules are well documented and numerous publications are available [16, 21, 49, 53, 54]. In this study, we focus eventually on the intercalation of LiCl alkali halide in the interlayer space of nacrite. Mode B has been adopted, firstly, due to hydrogen bonds between the oxygen atoms on the surface of the tetrahedral sheet of one layer and adjacent hydroxyl groups on the surface of the octahedral sheet of the next layer [55]. Secondly, this process ensures the fast intercalation of the alkali halide without destruction of the kaolinite framework and complications of the kaolinite/alkali halide interactions compared to Mode A. Finally, the protocol of synthesis followed in Mode B is much easier in comparison to that in Mode C. For these reasons, potassium acetate "KAc" was selected as a precursor for the expansion of nacrite [15, 49, 52]. The resulting KAc complex is characterized by a basal distance equal to 1.4 nm; it is then washed with water and air dried leading to a stable hydrate (0.84

nm), which constituted the starting material for the next step of the synthesis of the new hybrid material [15, 17, 20, 49].

4.1. The Intercalation Process of Lithium Chloride Alkali Halide in the Interlamellar Space of Nacrite

The inorganic salt employed during the course of this work was imposed by the literature data [52, 56], since the intercalation of lithium chloride alkali halide into kaolinite, in the previous cases, has failed due to the hygroscopic properties of the salt–clay mixture [57]. Thus, this research has been the first to intercalate LiCl in the interlamellar space of nacrite. Experiments based on the use of water as a solvent induces an unaccomplished intercalation of Li^+ cations. For this reason, different organic solvents (acetone, methanol, ethanol, glycerol, and ethylene glycol) were tried until an intercalation of 0.82 g of LiCl was reached in the presence of 20 ml of acetone at room temperature [49]. Indeed, acetone is considered as the best solvent for nacrite intercalation after 3 days of mechanical shaking under a magnetic stirrer. The final hybrid product was obtained and labeled: nacrite–LiCl [49].

4.2. Structural Characterization of Nacrite–LiCl Nanohybrid Material

The intercalation process is characterized via X-ray diffraction analysis, thermogravimetric analysis, infrared spectroscopy, and electrochemical impedance spectroscopy. In the following sections, the structural properties of nacrite–LiCl hybrid will be detailed starting with X-ray diffraction analysis.

4.2.1. X-ray Measurements

4.2.1.1. Qualitative XRD Analysis

By examining the *00l* reflections of the XRD pattern related to the stable nacrite–LiCl hybrid, Figure 6, we note a main reflection situated at 7.724°2θ, with d_{002}= 1.143± 0.002 nm basal spacing value attributed to an expansion of the interlamellar space of nacrite by ~0.423 nm along the ***c**** axis. This result is probably due to the insertion of lithium chloride salt accompanied by one water sheet into the nacrite matrix [49]. The exploitation of the CV coefficient and the rationality series confirm the homogenous sample character [49].

However, the high *FWHM* value at around 0.846°2θ of the first reflection is interpreted as a contradictory result. This is traduced by the fact that the ***FWHM*** could be notably affected by stress, strain, and interstratifications [49]. The extent of intercalation was determined using integrated areas of the reflections [58]:

$$\text{Intercalation ratio} = \left[\frac{I_{002}\ \text{hybrid}}{I_{002}\ \text{hybrid} + I_{002}\,\text{nacrite}}\right] \times 100\% \quad (5)$$

where I_{002}hybrid and I_{002}nacrite represent the main basal peak intensity of the hybrid and of the unexpanded nacrite component (d_{002} ~ 0.72 nm), respectively. The intercalation ratio value is equal to 86% for nacrite–LiCl and remained unchanged even for long time reaction.

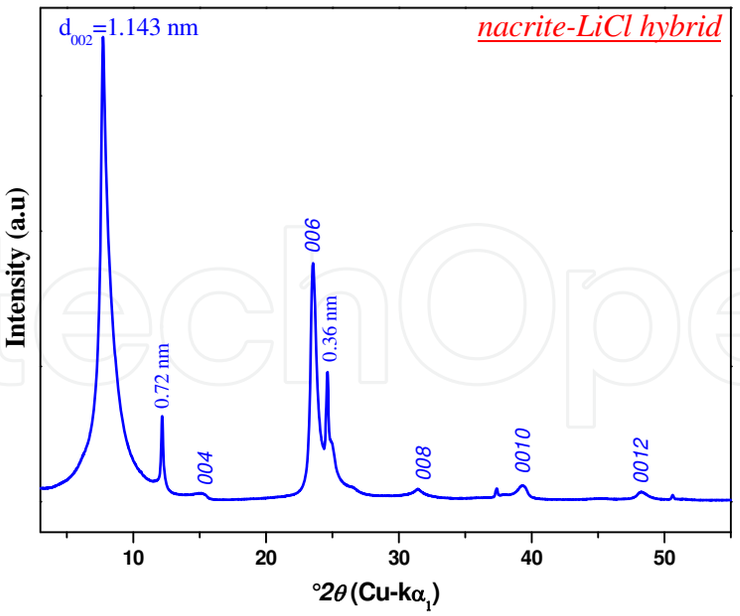

Figure 6. Experimental XRD pattern of the nacrite–LiCl hybrid [49].

4.2.1.2. Quantitative XRD Analysis

Simulations of the *00l* reflections seem to be a dominant path to gain an accurate picture about the fine structure of the nacrite–LiCl hybrid including the number and positions of the intercalated species in the interlayer space of nacrite. For that, an XRD-modeling computer program designed to carry out intensity calculations was used: The quantitative XRD analysis is based essentially on comparison between the experimental XRD pattern with the theoretical one [49].

However, the tiny atomic scattering factor of $Li^+(2)$ prevents the location of this cation with good preciseness in the interlamellar space of nacrite. So, we dressed a series of models with different positions of Li^+ cation [49]. It was therefore interesting to handle the unweighted R_p factor of each model as an indication of the effectiveness of fit [59]:

$$R_p = \sqrt{\frac{\sum\left[I(2\theta_i)obs - I(2\theta_i)calc\right]^2}{\sqrt{\left[I(2\theta_i)obs\right]^2}}} \quad (6)$$

where, $\boldsymbol{I(2\theta_i)obs}$ and $\boldsymbol{I(2\theta_i)calc}$ represent measured and calculated intensities, respectively, at the $2\theta_i$ position, the subscript **i** running over all points in the refined angular range. R_p is mainly influenced by the most intense diffraction maxima, such as the *00l* reflections, which contains essential information on the proportions of the different layer types and layer thickness [49].

The best model belongs to the smallest R*p* factor (6.20%) [49]. This model suggests the presence of a hydrated salt and is in agreement with the qualitative analysis. It allows then a more

accurate determination of the structural parameters of the stable nacrite–LiCl hybrid per half unit-cell: The *z* coordinates of intercalated Li^+ and Cl^- cations, taken from the oxygen surface oxygen along the normal to the layer, are respectively, 0.96 ± 0.01 nm and 0.64 ± 0.01 nm along c* axis. Finally, one intercalated water molecule situated at $z = 0.79 \pm 0.01$ nm is sandwiched between the cation and the anion [49].

To summarize, the intercalated species stand vertically in the interlayer space of nacrite, where the cations are located close to the ditrigonal holes of the tetrahedral layers and the anions are located close to the inner-surface hydroxyls of the octahedral layer of the subsequent sheet [49]. Moreover, the quantitative study of the nacrite–LiCl hybrid clearly showed an interstratified stacking characterized by a segregation tendency consisting of a total demixion of two types of layers: Layer A related to a minor fraction (14%) of the unexpanded 0.72 nm clay and Layer B attributed to a major fraction (86%) of the intercalated nacrite $\{W_A = 0.86, W_B = 0.14, P_{AA} = 1, P_{AB} = 0, P_{BA} = 0, P_{BB} = 1\}$[49]. The structural formula of the studied hybrid at room temperature was then determined as $\{(1-\alpha)[Si_2Al_2O_5(OH)_4LiCl.H_2O] + \alpha[Si_2Al_2O_5(OH)_4]\}$ per half unit cell, where "α" is equal to 0.14 and corresponds to the unexpanded nacrite fraction [49].

4.3. IR Spectroscopy

By comparing the spectrum of nacrite intercalated with lithium chloride to the spectrum of the untreated nacrite, it is possible to follow the modification of the stretching and deformation vibrations: they shift from their positions and their shapes change. These effects are a consequence of several factors, such as the intercalated entities, the degree of intercalation, and the degree of hydration [60].

These modifications are manifested in the recorded spectrum of the nacrite–LiCl hybrid [49].

Finally, IR spectroscopy proved that the intercalating species overcome the strong interactions between the nacrite-like layers and form hydrogen bonds with components of the TO layer [49]:

1. The Cl^- halide anion interacts with the inner surface hydroxyls through hydrogen-bonding;
2. The intercalated water molecule only interacts with the Cl^- and Li^+ ions;
3. The Li^+ alkali cation, located near the basal oxygens of the nacrite layer, interacts electrostatically with the negatively charged oxygens of the inner-surface oxygen.

These results are in concordance with those suggested by [50, 51, 60–62].

4.4. Thermal Analysis: Decomposition Process of the Nacrite–LiCl Nanohybrid During Heat Treatment

Thermogravimetric analysis of the nacrite–LiCl hybrid reveals that the sample gradually loses weight from room temperature to 800°C (Scheme 1) [49]:

1. The first remarkable weight loss was observed between 298 and 423 K and is mostly attributed to the drying process by which the water molecules that are confined to the clay mineral pores are released.

2. The second weight loss (3.62%) occurred between 673 and 773 K and belongs to the removal of the intercalated water molecule. This temperature range is also characterized by the beginning of the dehydroxylation of the hybrid at around 723 K. The chemical decomposition reaction of the hybrid per half unit cell can be expressed as follows:

$$\{(1-\alpha)\,[Si_2Al_2O_5(OH)_4.LiCl] + \alpha[Si_2Al_2O_5(OH)_4]\}$$
$$\rightarrow \{(1-\alpha)[Si_2Al_2O_7.LiCl] + \alpha[Si_2Al_2O_7]\} + \{2(1-\alpha)\,H_2O + 2\alpha H_2O\}.$$

The product formed at the commencement of the dehydroxylation of the hybrid is called "metanacrite–LiCl hybrid": { $Si_2Al_2O_7$.(1-α)LiCl }, (α = 0.14), and is amorphous.

3. The third weight loss was centered on 873 K (9.23%) and was due to the removal of two structural water {2(1-α) H_2O + 2α H_2O} = {2 H_2O} during the calcination process. This step was ultimately accompanied by the evolution of the hydrogen halide which results from the following thermal hydrolysis [63, 64]:

$$2SiO_2.Al_2O_3 + (1-\alpha)\,LiCl \rightarrow 2SiO_2.Al_2O_3.\frac{(1-\alpha)}{2}$$
$$Li_2O + (1-\alpha)\,HCl - \frac{(1-\alpha)}{2}H_2O.$$

On the clay surface, a liberated water molecule associates with Cl^- to form volatile HCl. The volatilization of HCl is responsible for a great amount of thermal mass loss of the examined hybrid. This phenomenon causes the trapping of the alkali metal oxide Li_2O within the metanacrite matrix. The amorphous hybrid phase formed during this step has the following chemical formula: {$Si_2Al_2O_7$. $(1-\alpha)$ /2Li_2O}. Knowing that $(1-\alpha)/2$ coefficient is equal to 0.43 ~ 0.5, we can simplify this chemical formula and express our "metanacrite–Li_2O hybrid" by the following formula {$Si_2Al_2O_7$. 1/2Li_2O} [49].

4.5. Electrochemical Characterization of Nacrite–LiCl Nanohybrid Material

Over the past three decades, much attention has been paid to solid electrolytes instead of liquid electrolytes because of their potential use in the electrochemical power sources (batteries, lithium ion cells, lithium batteries, fuel cells, electrochemical sensors, etc.) [65]. The advantages of solid electrolytes include longer life, high energy density, and no possibility of leak, etc. They are suitable in compact power batteries used in pace-makers, mobile telephones, and laptops [66]. In order to improve the bulk properties of solid electrolytes, a good number of researchers are interested in the synthesis and characterization of lithium-ion conductors based on different classes of materials such as ceramics, polymers, glasses, and so on [65, 30]. They are motivated by the small ionic radius of Li^+ cation, its low weight, ease of motion, and its appliance in high energy density batteries [67–71]. Therefore, we are proposing to innovate a new class of conductors based on nacrite-polytype clay [30].

http://dx.doi.org/10.5772/61594

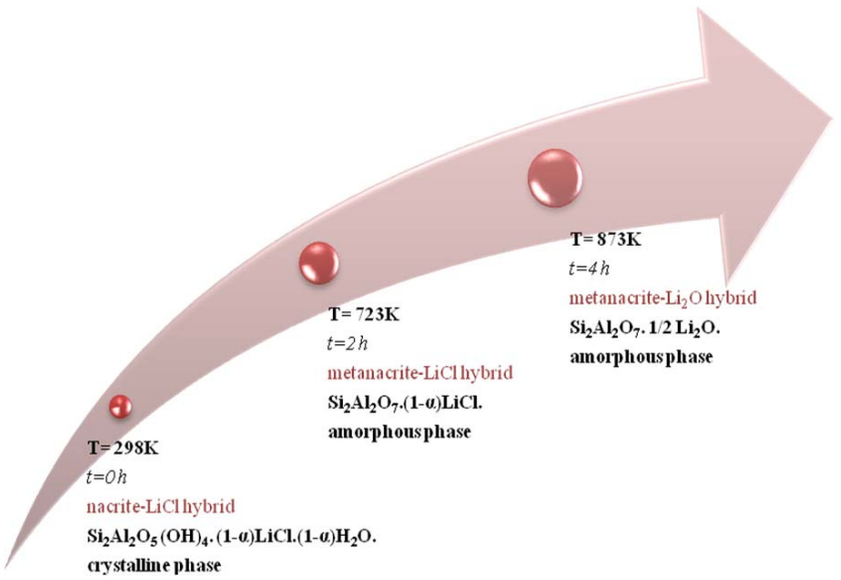

Scheme 1. Schematic representation of the thermal transformations of heat-treated nacrite–LiCl hybrid from room temperature to 873K [30].

4.5.1. Impedance Analysis

With the $((-Z''))$ versus Z' representations (Figure 7), we observed the existence of semicircles in the complex plane from 548 K to 873 K. At high temperature, these semi-arcs shift toward higher frequencies with a significant reduction of their size. We point out that nacrite–LiCl hybrid becomes more conductive at high temperature. We think that this phenomenon is attributed to the existence of a deformation (destruction) of some physical characteristics of the host clay material framework and to some chemical characteristics of LiCl alkali halide [30].

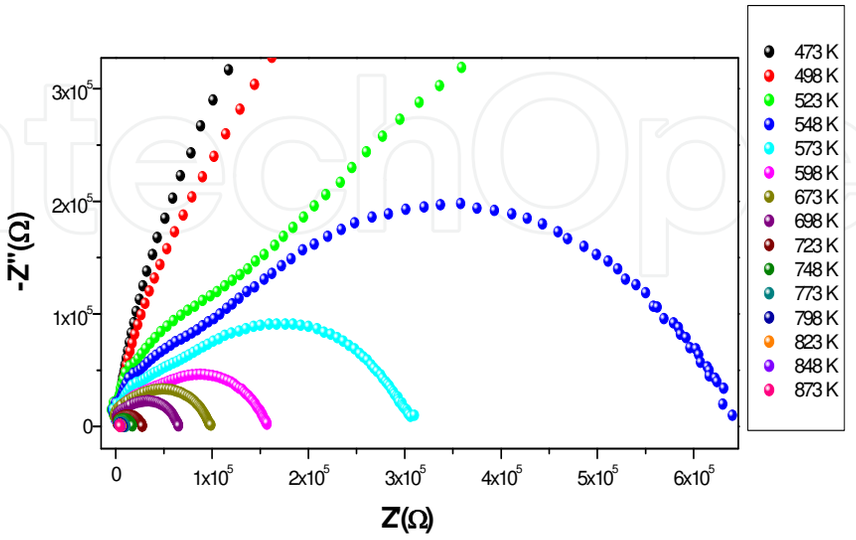

Figure 7. Nyquist diagram of nacrite–LiCl hybrid at a temperature range from 473 to 873 K [30].

4.5.2. Electrical Conductivity

The σ_{dc} of nacrite–LiCl hybrid increases from ($4.02 \cdot 10^{-6}$ S.m^{-1}) at 523 K to the ($0.11 \cdot 10^{-2}$ S.m^{-1}) at 873 K. An Arrhenius behavior was observed for the hybrid. The $E_{a(dc)}$ was determined from the slope of log ($\sigma_{dc}.T$) versus(1000 /T) and was found to be 0.84 eV and 0.82 eV, respectively, below and above 673 K [30]. The obtained values suggest an ionic conduction process. The *ac* conductivity measurements at high frequencies (1 MHz) show that σ_{ac} increases from $1.22 \cdot 10^{-4}$ S.m^{-1} at 523 K to $0.13 \cdot 10^{-2}$ S.m^{-1} at 873 K. This remarkable increase is also related to the increase of the number of free ions in the hybrid matrix in terms of temperature [30]. The $E_{a(ac),}$ calculated in agreement with (Eq.(3)), corresponds to the free energy barrier that an ion has to overcome for a successful jump from one site to another. These values designate that the ionic transport mechanism can be interpreted by the thermally activated hopping process [72].

According to these experimental results, we deduce that the disordered hybrid bears easier motion than the ordered one [30]. We conclude that contribution of disorder and defects in the hybrid framework are responsible for the motion of charge carriers; this result is in agreement with the previous publication of Kumar and Yashonath [66, 30].

Furthermore, Li^+ is known as an excellent current carrying ion in superionic solids motivated by its small ionic radius of 0.076 nm, lower weight, and ease of motion [66], but Cl^- anion appears to be rather less mobile than the cation due to its great ionic radius equal to 0.181 nm [66].

To conclude, Li^+ is the common current carrier via hopping from one site to the next for both "metanacrite–LiCl hybrid" and "metanacrite–Li_2O hybrid". Since the "metanacrite–Li_2O hybrid" phase is more amorphous than the "metanacrite–LiCl hybrid" phase, therefore it produces greater ionic conductivity. This shows that the conductivity was preferably affected by the amorphicity of the metanacrite framework through which mobile lithium ions may migrate.

$Si_2Al_2O_7 \cdot \frac{1}{2} \cdot L\ i_2O$ hybrid's high conductivity (σ_{ac}~ 10^{-2} S.m^{-1}) makes it an excellent candidate as electrolyte solid for lithium-ion batteries. Furthermore, this amorphous-type Li-ion conductor offers several advantages such as low cost and ease of handling. Its use instead of the conventional superionic conductors can drastically improve the safety aspects of lithium batteries [30].

5. Concluding Remarks

The structural and electrical properties of metanacrite synthesized from Tunisian nacrite were investigated in the first part of this work. The amorphous character of metanacrite was identified using XRD, IR, TEM, and EDXS analysis. Results of the electrochemical impedance spectroscopy show that the amorphous sample behaves like a semiconductor material. The present work gives possible valorization of Tunisian metanacrite as an interesting precursor to produce a new class of cementitious materials [29]. In the second part, structural experiments have been conducted in order to characterize the salt intercalation process between the nacrite

layers. The stable intercalated material has been characterized by XRD, TG, and IR analyses. The XRD pattern showed basal spacing at 1.143± 0.002 nm with integral series of 00*l* reflections, indicating an ordered structure of parallel 1:1 layers. The quantitative XRD analysis showed that best agreement between the observed and simulated patterns (R*p* = 6.20%) was obtained with one Cl^- ion at $z = 0.64 \pm 0.01$ nm, one Li^+ ion at $z = 0.96 \pm 0.01$ nm and one H_2O at $z = 0.79 \pm 0.01$ nm in the interlamellar space of nacrite (per half-unit cell). The Li^+ cation was located near the oxygen atom plane while the Cl^- anion was near the hydroxyl groups of the adjacent layer. The TG analysis of the hybrid produced showed a loss of water between 723 and 873 K, the weight loss (1 molecule per half unit cell) corresponding to the interlamellar water, in agreement with that showed by XRD. The positions of the H_2O molecules, Li^+ and Cl^-, suggest an interaction between Li^+ and the basal oxygen on one side and Cl^- and the surface hydroxyls on the other side. The H_2O can establish binding either with Li^+ cation or Cl^- ions [49]. The investigation of the *ac* and *dc* conductivity of nacrite–LiCl hybrid suggests that the suppression in the degree of crystallinity of the elaborated hybrid improves dramatically the ionic conduction, which is about ten orders of magnitude larger than the low temperature conductivity value. The activation energies for conduction measured at different temperatures indicate that the conduction mechanism is driven by hopping of Li^+ ions from one site to the neighboring one [30].

Finally, Tunisian nacrite is a candidate for the production of metanacrite as a supplementary cementitious material and as a host material of nanohybrid owing to its high crystallinity and unique structure. Further studies are in progress to point out the use of nacrite to synthesize other materials for a wide range of applications.

Author details

Nouha Jaafar*, Hafsia Ben Rhaiem and Abdesslem Ben Haj Amara

*Address all correspondence to: nouhajaafar@yahoo.fr

Laboratory of Physics of Lamellar Hybrid Materials and Nanomaterials, Department of Physics, Faculty of Sciences, Bizerte, University of Carthage, Tunis, Tunisia

References

[1] Hu XL, Michaelides A. The kaolinite (001) polar basal plane. Surf Sci 2010;604:111–7.

[2] Miranda-Trevino JC, Coles CA. Kaolinite properties, structure and influence of metal retention on pH. Appl Clay Sci 2003;23:133–9.

[3] Newman ACD. Chemistry of clays and clay minerals, Mineral. Soc. Engl. Monogr. Longman, Essex, England. p. 6. 1987.

[4] Liew YM, Kamarudin H, Mustafa Al Bakri AM, Luqman M, Khairul Nizar I, Ruzaidi CM, Heah CY. Processing and characterization of calcined kaolin cement powder. Construct Build Mater 2012;30:794–802.

[5] Bear FE. Chemistry of the Soil, 2nd edn. Reinhold Publishing, New York. 1965.

[6] Cruz M, Jacobs J, Fripiat JJ. International Clay Conference Madrid. 1972;1:59.

[7] Giese RF. Clays Clay Miner 1973;21:145.

[8] Wolfe RW, Giese RF. Clays Clay Miner 1974;22:139.

[9] Gupta SS, Krishna GB. Removal of Cd(II) from aqueous solution by kaolinite, montmorillonite and their poly(oxo zirconium) and tetrabutylammonium derivatives. J Hazard Mater 2006;128:247–57.

[10] Sarma YC, Prasad C, Rupainwar DC. J Ind Assoc Environ Manage 1991;18:100.

[11] Yavuz O, Altunkaynak Y, Guzel F. Removal of copper, nickel, cobalt and manganese from aqueous solution by kaolinite. Water Res 2003;37:948–52.

[12] Heller-Kallai L, Lapides I. Reactions of kaolinites and metakaolinites with NaOH-comparison of different samples (Part 1). Appl Clay Sci 2007;35:99–107.

[13] Siddique R, Klaus J. Influence of metakaolin on the properties of mortar and concrete: a review. Appl Clay Sci 2009;43:392–400.

[14] Gardolinski JE, Peralta-Zamora P, Wypch FJ. Colloid Interface Sci 1999;211:137.

[15] Ben Haj Amara A. X-ray diffraction, infrared and TGA/DTG analysis of hydrated nacrite. Clay Miner 1997;32:463–70.

[16] Ben Haj Amara A, Ben Brahim J, Besson G, Pons CH. Study of intercalated nacrite with dimethylsufoxide and n-methylacetamide. Clay Miner 1995;30:295–306.

[17] Ben Haj Amara A, Ben Brahim J, Ben Ayed N, Ben Rhaiem H. Occurence of nacrite in old Pb-Zn deposits from northern Tunisia. Clay Miner 1996;31:127–30.

[18] Ben Haj Amara A, Ben Brahim J, Plançon A, Ben Rhaiem H, Besson G. Etude Structurale d'une Nacrite Tunisienne. J Appl Crystallograph 1997;30:338–44.

[19] Ben Haj Amara A, Plançon A, Ben Brahim J, Ben Rhaiem H. XRD Study of the stacking mode in natural and hydrated nacrite. Mater Sci Forum 1998a;278–81:809–13.

[20] Ben Haj Amara A, Ben Brahim J, Plançon A, Ben Rhaiem H. X-Ray Diffraction study of the stacking modes of hydrated and dehydrated nacrite. J Appl Crystallograph 1998b;31:654–62.

[21] Ben Haj Amara A, Ben Rhaiem H, Plançon, A. Structural evolution of nacrite as a function of the nature of the intercalated organic molecules. J Appl Crystallograph 2000;33:1351–9.

[22] Bailey SW. Polymorphism of the kaolin minerals. Am Mineralog 1963;48:1197–209.

[23] Leluk K, Orzechowski K, Jerie K, Baranowski A, SŁonka T, GŁowinski J. Dielectric permittivity of kaolinite heated to high temperatures. J Phys Chem Solids 2010;71:827–31.

[24] Anthony GD, Garn PD. Kinetics of kaolinite dehydroxylation. J Am Ceramic Soc 1974;57:132–5.

[25] McManus J, Ashbrook SE, MacKenzie KJD, Wimperis S. ^{27}Al multiple-quantum MAS and 27Al^{1}H CPMAS NMR study of amorphous aluminosilicates. J Non-Crystall Solids 2001;282:278–90.

[26] Sabir B, Wild S, Bai, J. Metakaolin and calcined clays as pozzolans for concrete: a review. Cement Concrete Compos 2001;23(6):441–54.

[27] Mielenz RG, White LP, Glantz OJ. Effect of calcination on natural pozzolanas. Am Soc Test Mater Special Technical Publication. 1950;99:43–91.

[28] Chakchouk A, Samet B, Mnif T. Study on the potential use of Tunisian clays as pozzolanic material. Appl Clay Sci 2006;33:79–88.

[29] Jaafar N, Ben Rhaiem H, Ben Haj Amara A. Correlation between electrochemical impedance spectroscopy and structural properties of amorphous Tunisian metanacrite synthetic material. Adv Mater Sci Eng 2014a;1–10. Article ID: 469871. http://dx.doi.org/10.1155/2014/469871

[30] Jaafar N, Naamen S, Ben Rhaiem H, Ben Haj Amara A. Elaboration of amorphous-clay hybrid: ($Al_2Si_2O_7$. 1/2 Li_2O) designed as a single ion conducting solid electrolyte for Li-ion batteries. Am J Anal Chem 2014b;5:1261–72. http://dx.doi.org/10.4236/ajac.2014.517132

[31] Austin IG, and Mott NF. Polarons in crystalline and noncrystalline materials. Adv Phys 1969;18:41–102.

[32] Pollak M. On the frequency dependence of conductivity in amorphous solids. Philos Magaz 1971;23(183):519–42.

[33] Pike GE. AC conductivity of scandium oxide and a new hopping model for conductivity. Phys Rev B 1972;6(4):1572–80.

[34] Elliott SR. A theory of A.C. conduction in chalcogenide glasses. Philos Magaz 1977;36:1291–304.

[35] Elliott SR. A.C. conduction in amorphous chalcogenide and pnictide semiconductors. Adv Phys 1987;36:135–218.

[36] Springett, BE. AC conductivity of 4.5 TiO_2–x $2P_2O_5$. J Non-Crystall Solids 1974;15:179–90.

[37] Giuntini JC, Deroide B, Belougne P, Zanchetta JV. Numerical approach of the correlated barrier hopping model. Solid State Commun 1987;62:739–42.

[38] Bensimon Y, Giuntini, JC, Belougne, P, Deroide, B, Zanchetta JV. An example of A.C. conduction by correlated barrier hopping in amorphous molybdenum sulphides. Solid State Commun 1988;68:189–92.

[39] Hummel RE. Electronic Properties of Materials, Springer, New York, NY, USA.1993.

[40] Nefzi H, Sediri F, Hamzaoui H, Gharbi N. Dielectric properties and electrical conductivity of the hybrid organic-inorganic polyvanadates $(H_3N(CH_2)_4NH_3)[V_6O_{14}]$. J Solid State Chem 2012;190:150–6.

[41] Deng Y, Norman White G, Dixon J. Effect of structural stress on the intercalation rate of kaolinite. J Colloid Interface Sci 2002;250(2):379–93.

[42] Vagvolgyi V, Kovacs J, Horvath E, Kristof J, Mako E. Investigation of mechanochemically modified kaolinite surfaces by thermoanalytical and spectroscopic methods. J Colloid Interface Sci 2008;317:523–9.

[43] Michaelian KH, Lapides I, Lahav N, Yariv, Brodsky I. Infrared study of the intercalation of kaolinite by caesium bromide and caesium iodide. J Colloid Interface Sci 1998;204:389–93.

[44] Martens WN, Frost RL, Kristof J, Horvath E. Modification of kaolinite surfaces through intercalation with deuterated dimethylsulfoxide. J Phys Chem B 2002;106(16):4162–71.

[45] Horvath E, Kristof J, Frost RL, Mako E, Jakab E, Rédey A. Identification of super-active centers in thermally treated formamide intercalated kaolinite. J Colloid Interface Sci 2005;289:132–8.

[46] Frost RL, Kristof J, Horvath E, Kloprogge JT. J Colloid Interface Sci 1999;214:109.

[47] Komori Y, Sugahara Y, Kuroda K. A Kaolinite-NMF-methanol intercalation compound as a versatile intermediate for further intercalation reaction of kaolinite. J Mater Res 1998;13:930–4.

[48] Zhang B, Li Y, Pan X, Jia X, Wang X. Intercalation of acrylic acid and sodium acrylate into kaolinite and their in situ polymerization. J Phys Chem Solids 2007;68(2):135–42.

[49] Jaafar N, Naamen S, Ben Rhaiem H, Ben Haj Amara A. Functionalization and structural characterization of a novel nacrite-LiCl nanohybrid material. Am J Anal Chem (Special Issue on X-Ray Diffraction). 2015;6:202–15. http://dx.doi.org/10.4236/ajac.2015.63019

[50] Michaelian KH, Yariv S, Nasser A. Study of the interactions between caesium bromide and kaolinite by photoacoustic and diffuse reflectance infrared spectroscopy. Can J Chem 1991a;69:749–54.

[51] Michaelian KH, Friesen WI, Yariv S, Nasser A. Diffuse reflectance infrared spectra of kaolinite and kaolinite/alkali halide mixtures. Curve-fitting of the OH stretching region. Can J Chem 1991b;69:1786–90.

[52] Lapides I, Lahav N, Michaelian KH, Yariv S. X-ray study of the thermal intercalation of alkali halides into kaolinite. J Thermal Analys 1997;49:1423–32.

[53] Naamen S, Ben Rhaiem H, Ben Haj Amara, A. XRD study of the nacrite/CsCl/H_2O intercalation complex. Mater Sci Forum 2004a;443–444:59–64.

[54] Naamen S, Ben Rhaiem H, Karmous, MS, Ben Haj Amara A.XRD study of the stacking mode of the nacrite/alkali halides complexes. Mater Struct 2004b;11.

[55] Giese RF. Interlayer bonding in kaolinite, dickite and nacrite. Clays Clay Miner Pergamon Press. Printed in Great Britain. 1973;21:145–9.

[56] Weiss A, Thielepape W, Orth H. Neue Kaolinit-Einlagerungsverbindungen. In: Rosenquist, T. and Graff-Petterson, P. (Eds.) Proc Int Clay Conf Israel University Press, Jerusalem. 1966;1:277–93.

[57] Garrett WG, Walker GF. The cation-exchange capacity of hydrated halloysite and the formation of halloysite-salt complexes. Clay Miner 1959;4:75–80.

[58] Wiewióra A, Brindley GW. Potassium acetate intercalation in kaolinites and its removal: effect of material characteristics. In Heller L. (Ed.) Proc Int Clay Conf, Israel University Press, Jerusalem. 1969;1723–33.

[59] Howard SA, Preston KD. Profile fitting of powder diffraction patterns. In: Bish DL, Post JE. (Eds.) Modern Powder Diffraction: Reviews in Mineralogy. Mineralogical Society of America, Washington DC. 1989, pp. 217–275.

[60] Yariv S, Lapides I, Michaelian KH, Lahav N. Thermal intercalation of alkali halides into kaolinite. J Thermal Analys Calorimetr 1999;56:865–84.

[61] Yariv S. Interactions of minerals of the kaolin group with cesium chloride and deuteration of the complexes. Int J Trop Agri 1986;5:310–22.

[62] Frost RL, Kristof J, Horvath E, Kloprogge JT. Spectrochim Acta A 2000;56:1191.

[63] Heller-Kallai L. Reactions of salts with kaolinite at elevated temperatures. Clay Miner 1978;13:221–35.

[64] Gabor M, Poeppl L, Koeros E. Effect of ambient atmosphere on solid state reaction of kaolin-salt mixtures. Clays Clay Miner 1986;34:529–33.

[65] Minami T, Tatsumisago M, Iwakura C, Kohjiya S, Tanaka I. Solid State Ionics for Batteries. Springer, Berlin, 2005.

[66] Kumar PP, Yashonath S. Ionic conduction in the solid state. J Chem Sci 2006;118:135–54.

[67] Ghosh A, Kofinas P. PEO based block copolymer as solid state lithium battery electrolyte. ECS Transac 2008;11:131–7.

[68] Wang M, Zhao F, Guo Z, Dong S. Poly(vinylidene fluoride-hexafluoropropylene)/organo-montmorillonite clays nanocomposite lithium polymer electrolytes. Electrochim Acta 2004;49:3595–602.

[69] Morenoa M, Quijadad R, Anaa MAS, Benaventea E, Romeroe PG, Gonzáleza G. Electrical and mechanical properties of poly(ethylene oxide)/intercalated clay polymer electrolyte. Electrochim Acta 2011;58:112–8.

[70] He P, Chen B, Wang Y, Xie Z, Dong F. Preparation and characterization of a novel organophilic vermiculite/poly(methyl methacrylate)/1-butyl-3-methylimidazolium hexafluorophosphate composite gel polymer electrolyte. Electrochim Acta 2013;111:108 –13.

[71] Prasanth R, Shubha N, Hng HH, Srinivasan M. Effect of nano-clay on ionic conductivity and electrochemical properties of poly(vinylidene fluoride) based nanocomposite porous polymer membranes and their application as polymer electrolyte in lithium ion batteries. Eur Polymer J 2013;49:307–18.

[72] Réau JM, Rossignol S, TanguyB, Rojo JM, Herrero P, Rojas RM, Sanz J. Conductivity relaxation parameters of some Ag^{+} conducting tellurite glasses containing AgI or the $(AgI)_{0.75}$ $(T1I)_{0.25}$ eutectic mixture. Solid State Ionics 1994;74:65–73.